https://doi.org/10.1016/j.renene.2023.04.090

Two-phase analytical modeling and intelligence parameter estimation of proton exchange membrane electrolyzer for hydrogen production

Bowen Wang[a,b,c], Meng Ni[b,*], Shiye Zhang[a], Zhi Liu [a,c], Shangfeng Jiang[d], Longhai Zhang[d], Feikun Zhou[e,*], Kui Jiao[a,c,*]

a. State Key Laboratory of Engines, Tianjin University, 135 Yaguan Road, Tianjin 300350, China

b. Department of Building and Real Estate, Research Institute for Sustainable Urban Development (RISUD), Research Institute for Smart Energy (RISE), The Hong Kong Polytechnic University, Hung Hom, Kowloon, Hong Kong, China

c. National Industry-Education Platform of Energy Storage, Tianjin University, 135 Yaguan Road, Tianjin 300350, China

d. Yutong Bus Co.Ltd.,Yutong Industrial Park, Yutong Road, Zheng zhou, Henan Province,450000,China

e. School of Mechatronic Engineering and automation, Foshan University, Foshan, 528000, China

*Corresponding authors: meng.ni@polyu.edu.hk; feikun_zhou@163.com; kjiao@tju.edu.cn

Abstract

The proton exchange membrane electrolyzer (PEME) is a promising tool for hydrogen production, and internal two-phase transport significantly influences its performance. In this study, a two-phase analytical PEME model incorporating the liquid saturation jump effect was developed, and intelligent parameter estimation using a genetic algorithm was proposed to achieve high-efficiency model validation. In-house experiments and experimental results from numerous papers in the literature were employed to prove the effectiveness of the proposed intelligent parameter estimation. Moreover, the two-phase simulation results demonstrated that the PEME voltage increased significantly when the current density reached the limiting value, and the liquid saturation in the anode catalyst layer (ACL) dropped to nearly zero. Increasing ACL porosity, decreasing ACL permeability, and decreasing ACL thickness could increase the

limiting current density within the investigated range. The simulated limiting current density could be >5 A cm^{-2} through proper design of the ACL parameters. For high-pressure cathode operation, increasing the cathode pressure and membrane permeability generally benefits water management inside the PEME and therefore increases the limiting current density. This study provides critical support for the design of cells and operating conditions for future PEME studies.

Keywords: Proton exchange membrane electrolyzer; intelligence parameter estimation; two-phase characteristics; liquid saturation jump; anode catalyst layer; cathode high pressure.

1. Introduction

Hydrogen is a clean, renewable energy source. It is widely recognized that large-scale hydrogen utilization can achieve energy diversity, promote the decarbonization process, and buffer the worldwide greenhouse effect [1,2]. Achieving highly efficient, low-cost hydrogen production is a prerequisite for promoting hydrogen energy utilization. Water electrolysis for hydrogen production can be properly integrated with various renewable sources (i.e., fluctuating solar, wind, and hydroelectric sources) and is thus considered a promising method for the future [3]. Among the different types of water electrolyzers, the proton exchange membrane electrolyzer (PEME) has attracted increasing attention in recent years owing to its advantages such as high-current-density operation, high purity of the produced hydrogen, and simplicity of its system [4].

PEMEs have a sandwich structure consisting of an anode, a cathode, and a membrane; the anode or cathode side includes a flow field (channel), porous transport layer (PTL), and catalyst

layer (CL). In PEME operation, electricity is supplied to the cell. Liquid water is supplied and consumed at the anode, and oxygen is produced and removed. Hydrogen is produced at the cathode, and water can be transferred across the membrane to the cathode. The electrochemical reactions inside the PEME are as follows:

anode: $H_2O \rightarrow 2H^+ + \frac{1}{2}O_2 + 2e^-$

cathode: $2H^+ + 2e^- \rightarrow H_2$

overall: $H_2O + \text{electricity} \rightarrow H_2 + \frac{1}{2}O_2$

Owing to the supply of liquid water and the production of gaseous O_2, complex two-phase flow and mass transport can significantly influence PEME performance [5–9]. Yuan et al. [5] comprehensively reviewed studies on bubble evolution and two-phase transport inside PEMEs. They summarized the complex effect of bubble evolution in PEMEs: Although bubble evolution can reduce the mass transfer loss near the activation surface by reducing the local gas supersaturation, it can also increase the activation loss by covering the activation surface. Panchenko et al. [6] visualized the two-phase flow inside an anode PTL (APTL) via neutron imaging. They observed the pulsed characteristics of liquid-oxygen transport during long-term operation, which led to fluctuations in cell performance. Obvious mass transport congestion and unstable cell performance were observed when the stoichiometry ratio of the supplied liquid water was 100, whereas the phenomenon was mitigated when it was 350 and 600. They also observed more significant gas accumulation under the shoulder in the APTL than under the channel. Wang et al. [7] used a novel thin–tunable liquid–gas diffusion layer (TT-LGDL) as the APTL and observed the internal two-phase flow in situ using a transparent cell and a

high-speed camera. They found that the number of large bubble slugs decreased when using TT-LGDL rather than Ti felt as an APTL. The bubble density significantly increased for the TT-LGDL, and the bubble size decreased, which promoted bubble escape from the reaction sites. Majasan et al. [8] visualized the two-phase flow behavior in a flow-field plate using a transparent cell and a high-speed camera. Long, continuous bubble slugs were observed in a serpentine flow field. A PEME with a parallel flow field exhibited better performance at a higher current density than that with serpentine.

Experimental visualization is generally restricted by the use of specialized instruments and installations and is usually expensive and time-consuming. Numerical and simulation studies can also elucidate the two-phase characteristics at relatively low cost [10–15]. Falcão and Pinto [10] reviewed the main modeling studies and basic modeling methods of PEMEs with different degrees of complexity, focusing on empirical and semi-empirical models. Arbabi et al. [11] simulated the formation and propagation of oxygen bubbles inside an APTL using the volume-of-fluid method and compared the bubble breakthrough path with the experimental results. Wu et al. [12] and Xu et al. [13] proposed an integration method for the three-dimensional two-phase PEME full-cell model and volume-of-fluid model of the anode flow field. The two-phase characteristics and bubble slug in the anode flow field were simulated using the volume-of-fluid method, which was further applied in the full-cell model as a boundary condition at the interface between the flow field and the APTL. The simulated polarization curves exhibited better agreement with the experimental results than those of the single full-cell model. In addition to the complex three-dimensional model, analytical and

reduced-dimensional models can be used to predict the two-phase characteristics of PEMEs with a low computational overhead and high efficiency. Han et al. [14] developed a two-phase mathematical model for a PEME anode. The modeling results showed that the PEME voltage exhibited a sudden increase, when the current density reached a limiting value. Moreover, the influence of APTL parameters on the limiting current density was investigated. Increasing the APTL porosity, decreasing its contact angle, and decreasing its thickness can increase the limiting current density. Lee et al. [15] developed a pore network model to generate a realistic microstructure of PTLs in PEMEs via a stochastic algorithm and investigated the effects of PTL–catalyst-coated membrane (CCM) contact, pore size, and porosity on internal two-phase transport. Based on their numerical results, they proposed an optimized electrode design by adding a microporous layer between the PTL and the CCM to reduce the transfer resistance at the PTL–CCM interface and enhance cell performance. Therefore, the PEME model can predict the two-phase characteristics and connect them with PEME performance.

Validation with experimental results is necessary for PEME modeling [16–21]. There are many critical modeling parameters, and their values under different and complex conditions are very difficult to accurately obtain experimentally, especially for electrochemical parameters. Sartory et al. [16] developed a semi-empirical PEME model and fitted the empirical parameters to the experimental results. Garcia-Salaberri [17] developed a one-dimensional, two-phase, nonisothermal PEME model. Electrochemical parameters, such as the exchange current density of the anode, significantly influence PEME performance. Aouali et al. [18] developed electrochemical and thermodynamic models of PEMEs. The modeling results were compared

with the experimental results to determine the electrochemical parameters, including the exchange current densities, charge transfer coefficients, and membrane conductivity. Therefore, parameter estimation, that is, choosing the proper values of these parameters to guarantee model validation, is a critical process. However, manually adjusting these parameters is either inefficient or invalid.

In this study, a two-phase analytical model for a PEME was developed. The phenomenon of a liquid saturation jump that occurs at the interface of layers with different porous parameters in the electrode is introduced in the model. An intelligent method for parameter estimation that can achieve high efficiency and automatic model validation is then proposed. Moreover, the effects of the anode catalyst layer (ACL) and cathode high-pressure operation on PEME performance and its two-phase characteristics have been investigated.

2. Methods

2.1 Experimental

2.1.1 Materials

A commercial CCM (manufactured by Wuhan WUT HyPower Technology) was used in this study. It consists of a membrane of Nafion 115, an anode catalyst of IrO_2 with a loading of 2.0 mg cm^{-2}, and a cathode catalyst of Pt/C with a loading of 0.8 mg cm^{-2}. Titanium felt with an IrO_2 plating layer was used as the APTL. The initial porosity and thickness of the titanium felt are 0.5 and 260 μm, respectively. The plating solution was prepared using chloroiridic acid, sodium nitrate powder, and isopropanol under stirring, and the IrO_2 loading was set to 1.0 mg cm^{-2}. The titanium felt was initially treated with concentrated hydrochloric

acid at 60℃ to form titanium hydride on the surface to protect the base material. For the plating process, the titanium felt was covered by the solution and then dried in the oven at 60℃. This process was repeated until the solution was exhausted. Then, the titanium felt was heated in a muffle furnace, with the temperature gradually increased at 2℃ min^{-1} and then kept at 350℃ for 1 h to finish the APTL preparation. The anode flow-field plate was a gold-plated titanium plate with a parallel flow field. The cathode PTL (CPTL) and flow-field plate consisted of carbon paper (Toray, TGP-H-060) and a carbon plate with a parallel flow field, respectively. Some of the basic materials are presented in Figure 1.

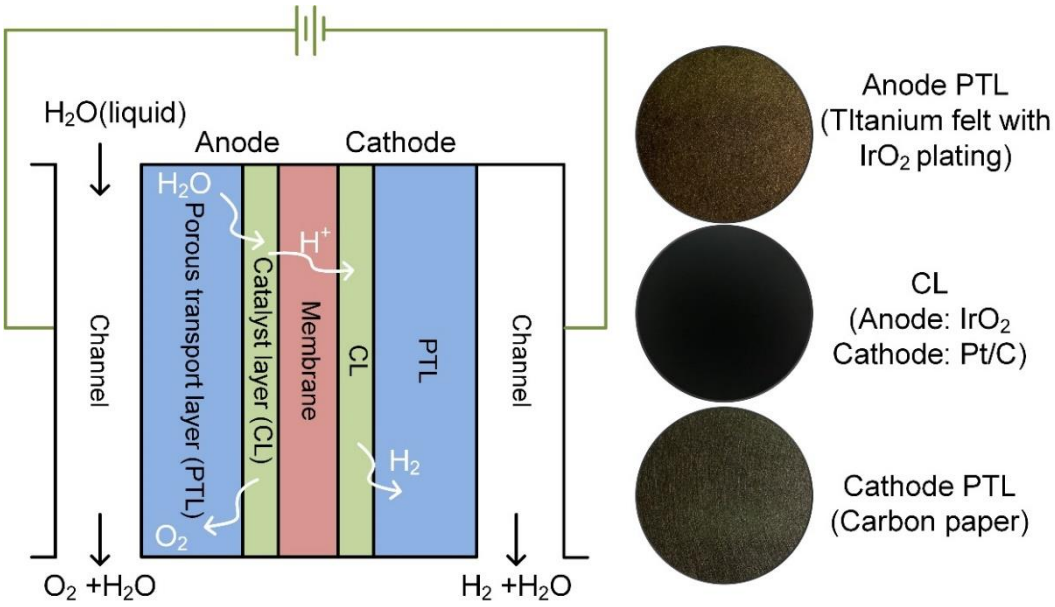

Figure 1. Schematic of the PEME model and basic materials.

2.1.2 Experimental setup

The PEME was prepared using end plates, current collector plates, flow-field plates, an APTL, a CPTL, and a CCM. The cell activation area was 5×5 cm^2. The torque was set at 2 N m to assemble the cells. The cell and experimental setup are shown in Supplementary Figure 1. Before the test, a leak test was conducted via pressure maintenance. The cell was connected

to a testing bench, and nitrogen was supplied to the anode and cathode at the dead end. The nitrogen supply was terminated when the inlet pressure reached 50 kPa. If the pressure drop was <2 kPa in 10 min, good gas tightness of the cell was achieved for further testing. A peristaltic pump supplied water to the cell, and a DC-regulated power supply supplied electricity. For the polarization curve test, the cell was operated in the constant-current mode. We recorded the voltage and current when the voltage remained constant for 2 min as a data point and then increased the current for the next point. An electrochemical station (Zahner Zennium E) was used for the electrochemical impedance spectroscopy (EIS) diagnosis. A sinusoidal current was adopted as the disturbance, and its amplitude and frequency range were 10% of the real-time current and 100 kHz to 0.1 Hz, respectively. The operating temperatures were 50℃, 65℃, and 80℃.

2.2 PEME two-phase model

A schematic of the PEME model is shown in Figure 1. The PEME includes an anode channel, an APTL, an ACL, a membrane, a cathode CL (CCL), a CPTL, and a cathode channel. To simplify the model, the following assumptions were made: The PEME operates in a steady and isothermal state, and the flow in the channels is laminar. The ideal gas law was applied to the gases at the anode and cathode. To simplify the complex gas–liquid two-phase flow in the channels, the velocity of the gas in the channels was taken to be the same as that in the liquid, and the pressure drop in the channels was neglected. The cathode gas was hydrogen with humidified water vapor.

2.2.1 Governing equations

Gas and liquid two-phase transport in the porous electrode is introduced in this section. Mass conservation can be expressed as

$$\nabla \cdot (\rho \boldsymbol{u}) = 0 \tag{1}$$

Momentum conservation in the porous electrode is simplified by using Darcy's law

$$\boldsymbol{u} = \frac{K_0 k}{\mu} \nabla p \tag{2}$$

Combining the above two equations of gas and liquid phases gives

$$\nabla \cdot \left(\rho_{\mathrm{lq}} \frac{K_0 k_{\mathrm{lq}}}{\mu_{\mathrm{lq}}} \nabla p_{\mathrm{lq}} \right) = 0 \tag{3}$$

$$\nabla \cdot \left(\rho_{\mathrm{g}} \frac{K_0 k_{\mathrm{g}}}{\mu_{\mathrm{g}}} \nabla p_{\mathrm{g}} \right) = 0 \tag{4}$$

$$k_{\mathrm{lq}} = {s_{\mathrm{lq}}}^4 \tag{5}$$

$$k_{\mathrm{g}} = \left(1 - s_{\mathrm{lq}}\right)^4 \tag{6}$$

where ρ (in kg m^{-3}) is the density, $\boldsymbol{u}$ (in m s^{-1}) is the velocity, K_0 (in m^2) is the intrinsic permeability of the porous medium, k is the relative permeability of the gas or liquid phase, μ (in N s m^{-2}) is the dynamic viscosity, p (in pascals) is the pressure, s is the saturation or volume fraction of the gas or liquid phase, and subscripts lq and g represent liquid and gas phases, respectively.

In porous media, the capillary pressure is the pressure difference between the gas and liquid pressures:

$$p_{\mathrm{c}} = p_{\mathrm{g}} - p_{\mathrm{lq}} \tag{7}$$

It can also be connected to liquid saturation through the Leverett function $J(s_{\mathrm{lq}})$:

$$p_c = \sigma_{lq} \cos\theta \left(\frac{\varepsilon}{K_0} \right)^{0.5} J(s_{lq}) \quad (8)$$

with

$$J(s_{lq}) = \begin{cases} 1.42\left(1-s_{lq}\right) - 2.12\left(1-s_{lq}\right)^2 + 1.26\left(1-s_{lq}\right)^3, & \theta<90^\circ \\ 1.42s_{lq} - 2.12{s_{lq}}^2 + 1.26{s_{lq}}^3, & \theta > 90^\circ \end{cases} \quad (9)$$

where p_c (in Pa) is the capillary pressure, σ_{lq} (in N m^{-1}) is the surface tension coefficient of liquid water, and θ (in degrees) and ε are the contact angle and porosity of the porous medium, respectively. The expression for the Leverett function differs for hydrophilic and hydrophobic surfaces. Porous electrodes generally consist of two different layers (PTL and CL) with different structural parameters. For the interface between the PTL and the CL, the values of the gas and liquid pressures are continuous, and the values of the liquid saturation on the two sides of the interface differ because of the different parameters of the two adjacent porous layers. This phenomenon is called the liquid saturation jump and is considered in the model.

2.2.2 Water crossover

Water transport across the membrane is a critical process inside the PEME that directly influences the species distributions at the anode and cathode. It is generally driven by three mechanisms: electro-osmotic drag (EOD), diffusion by the membrane water content difference, and hydraulic permeation by the liquid pressure difference between the anode and cathode. Their crossover fluxes can be calculated as follows:

$$J_{lq,cro} = J_{lq,hyd} + J_{lq,dmw} + J_{lq,nd} \quad (10)$$

$$J_{lq,nd} = n_d \frac{I}{F} \quad (11)$$

$$J_{lq,dmw} = \frac{\rho_m}{EW} \frac{D_{mw}\left(\lambda_a - \lambda_c\right)}{\delta_m} \quad (12)$$

$$J_{\mathrm{lq,hyd}} = c_{\mathrm{lq}} \frac{K_{\mathrm{m}}}{\mu_{\mathrm{lq}}} \frac{p_{\mathrm{lq,cl\text{-}mem,a}} - p_{\mathrm{lq,cl\text{-}mem,c}}}{\delta_{\mathrm{m}}} \quad (13)$$

where $J_{\mathrm{lq,cro}}$ (in mol $\mathrm{m^{-2}\ s^{-1}}$) is the total water crossover flux; $J_{\mathrm{lq,nd}}$, $J_{\mathrm{lq,dmw}}$, and $J_{\mathrm{lq,hyd}}$ (in mol $\mathrm{m^{-2}\ s^{-1}}$) are the water crossover fluxes by EOD, membrane water diffusion, and hydraulic permeation, respectively; n_{d} is the EOD coefficient; I (in A $\mathrm{m^{-2}}$) is the current density; F (= 96,485 C $\mathrm{mol^{-1}}$) is the Faraday constant; ρ_{m} (in kg $\mathrm{m^{-3}}$) is the density of the dry membrane; EW (in kg $\mathrm{mol^{-1}}$) is the equivalent weight of the membrane; D_{mw} (in mol $\mathrm{s^{-2}\ s^{-1}}$) is the diffusivity of membrane water; λ_{a} and λ_{c} are the membrane water content in ACL and CCL, respectively; δ_{m} (in meters) is the membrane thickness; c_{lq} (in kg $\mathrm{m^{-3}}$) is the liquid water density; K_{m} (in $\mathrm{m^2}$) is the permeability of the membrane; and $p_{\mathrm{lq,cl\text{-}mem,a}}$ and $p_{\mathrm{lq,cl\text{-}mem,c}}$ (in pascals) are the liquid pressure at the interface between the CL and membrane of the anode and cathode, respectively. The direction of $J_{\mathrm{lq,cro}}$ was from the anode to the cathode.

2.2.3 Electrochemical model

The input voltage of the PEME at a certain current density consists of reversible voltage, activation overpotential, and ohmic overpotential:

$$V = E_{\mathrm{oc}} + \eta_{\mathrm{act,a}} + \eta_{\mathrm{act,c}} + \eta_{\mathrm{ohm}} \quad (14)$$

where E_{oc} (in volts) is the reversible voltage, $\eta_{\mathrm{act,a}}$ and $\eta_{\mathrm{act,c}}$ (in volts) are the activation overpotentials of the anode and cathode, respectively, and η_{ohm} (in volts) is the ohmic overpotential.

The reversible voltage can be calculated by using the Nernst equation with a temperature correction:

$$E_{\mathrm{oc}} = 1.229 - 0.9\times10^{-3}\left(T - 298\right) + \frac{RT}{2F}\left[\ln\left(\sqrt{p_{\mathrm{a}}}\,p_{\mathrm{c}}\right)\right] \quad (15)$$

where V_{oc} (in volts) is the reversible voltage, T (in kelvins) is the temperature, and R (=8.31 J K^{-1} mol^{-1}) is the ideal gas constant.

The relationship between the current density and activation overpotential of the anode and cathode can be described by the Butler–Volmer equation [13]

$$I = s_{lq}^2 \cdot i_{0,a} \left(\exp\left(\frac{4\alpha_a F \eta_{act,a}}{RT} \right) - \exp\left(-\frac{4(1-\alpha_a) F \eta_{act,a}}{RT} \right) \right) \quad (16)$$

$$I = i_{0,c} \left(\exp\left(\frac{2\alpha_c F \eta_{act,c}}{RT} \right) - \exp\left(-\frac{2(1-\alpha_c) F \eta_{act,c}}{RT} \right) \right) \quad (17)$$

$$i_{0,a} = i_{ref,a} \exp\left(\frac{-7.6\times10^4}{R} \left(\frac{1}{T} - \frac{1}{298} \right) \right) \quad (18)$$

$$i_{0,c} = i_{ref,c} \exp\left(\frac{-1.8\times10^4}{R} \left(\frac{1}{T} - \frac{1}{298} \right) \right) \quad (19)$$

where s_{lq} represents the liquid saturation at the interface between the anode CL (ACL) and the membrane; $i_{0,a}$ and $i_{0,c}$ (in A m^{-2}) are the exchange current densities of the anode and cathode, respectively; α_a and α_c are the charge transfer coefficients of the anode and cathode, respectively; and $i_{ref,a}$ and $i_{ref,c}$ (in A m^{-2}) are the reference exchange current densities of the anode and cathode, respectively. The first and second terms in Eqs. 16 and 17 represent the forward and reverse reaction rates, respectively. When the PEME is used for hydrogen production, the forward reaction dominates, and the second item can be neglected. Therefore, the activation overpotential can be expressed as

$$\eta_{act,a} = \frac{RT}{4\alpha_a F} \ln\left(\frac{1}{s_{lq}^2} \frac{I}{i_{0,a}} \right) \quad (20)$$

$$\eta_{act,c} = \frac{RT}{2\alpha_c F} \ln\left(\frac{I}{i_{0,c}} \right) \quad (21)$$

The ohmic overpotential is mainly caused by proton conduction in the membrane resulting from the much smaller conductivity of protons than the electronic conductivity of the porous medium. Proton conduction in the ionomers of the CLs should also be considered, and the transport distance was assumed to be half of the CL thickness. Furthermore, titanium felt is a common material used in APTLs for PEMEs; it can generally cause non-negligible contact resistance, which is considered in the present study. The Ohmic overpotential was calculated using the Ohmic law

$$V_{\mathrm{ohm}} = \left(\frac{\delta_{\mathrm{mem}}}{\sigma_{\mathrm{m}}} + \frac{\delta_{\mathrm{cl,a}}}{2\sigma_{\mathrm{m,cl,a}}} + \frac{\delta_{\mathrm{cl,c}}}{2\sigma_{\mathrm{m,cl,c}}} + R_{\mathrm{con}} \right) I \tag{22}$$

where $\delta_{\mathrm{cl,a}}$ and $\delta_{\mathrm{cl,c}}$ are the thicknesses of the anode and cathode CLs, respectively; σ_{m} (in S m^{-1}) is the proton conductivity of the membrane; $\sigma_{\mathrm{m,cl,a}}$ and $\sigma_{\mathrm{m,cl,c}}$ (in S m^{-1}) are the proton conductivities in the ionomer of the anode and cathode CLs, respectively; and R_{con} (in $\Omega\,\mathrm{m}^2$) is the contact resistance inside the PEME. Membrane conductivity is related to water content and temperature; therefore, the following correlation of Nafion with the correction factor was applied to the model:

$$\sigma_{\mathrm{m}} = k_{\mathrm{m}} \times (0.5139\lambda - 0.326) \exp\left[1268 \left(\frac{1}{303} - \frac{1}{T} \right) \right] \tag{23}$$

$$\sigma_{\mathrm{m,cl}} = \sigma_{\mathrm{m}} \omega^{1.5} \tag{24}$$

where k_{m} is the correction factor for the proton conductivity of a detailed Nafion membrane and ω is the ionomer fraction of the CL.

2.2.4 Calculation procedure

Mass transport inside the PEME occurs mainly along the through-plane direction. Consequently, the governing equations can be simplified as one-dimensional transport. For the

boundary conditions, the gas pressures at the interfaces of the PTL and the channel in the anode and cathode were equal to the inlet pressures at the anode and cathode, respectively. The liquid saturation at the interfaces of the PTL and channel can be calculated using mass conservation and the assumed gas/liquid velocity ratio in the channels (see the Supplemental Information), and the liquid pressure can also be obtained. At the ACL–membrane interface, liquid water is consumed, oxygen is produced from the electrochemical reaction, and water is transported to the cathode across the membrane. Hydrogen is produced from the electrochemical reaction at the CCL–membrane interface. The crossover water is primarily transformed into saturated water vapor at the cathode, and the residual water is discharged in the liquid state. The discrete analytical equations are listed in Supplementary Table 1. The materials, operating parameters, and other transport parameters are listed in Supplementary Tables 2 and 3 [13,18,22–25].

2.3 Intelligence parameter estimation

To ensure good agreement between the simulation results and experimental data, a genetic algorithm (GA) was applied to execute a high-efficiency, accurate, and automatic estimation of the critical modeling parameters. In the model, six critical parameters are uncertain and need to be estimated: the reference exchange current densities of the anode and cathode, charge-transfer coefficients of the anode and cathode, correction factors for membrane conductivity, and contact resistance. The detailed procedure of the GA is shown in Supplementary Figure 2. The polarization curve and ohmic impedance are the two objectives to be measured; therefore, the fitness function f is constructed using the reciprocal of the sum of the squared errors of the two objectives:

$$f = \frac{1}{\sum_{I_{\min}}^{I_{\max}} \left(V\left(i_{ref,a}, i_{ref,c}, \alpha_a, \alpha_c, k_m, R_{con}\right) - V_{\exp} \right)^2 \cdot \sum_{I_{\min}}^{I_{\max}} \left(R\left(k_m, R_{con}\right) - R_{\exp} \right)^2} \quad (25)$$

where V (in volts) is the calculated voltage at a certain current density, which is a function of the six undetermined parameters; $V_{\exp}$ (in volts) is the experimental voltage at the current density; $R\ (\Omega\ \mathrm{m}^2)$ is the calculated ohmic impedance at a certain current density, which is a function of k_{m} and R_{con}; $R_{\exp}$ (in $\Omega\ \mathrm{m}^2$) is the experimental ohmic impedance at the current density; and $\sum_{I_{\min}}^{I_{\max}}$ represents the range of current densities in experiments. The range constraints of the six undetermined parameters, based on the literature [18,23], are listed in Supplementary Table 4. The GA program searches for a solution to maximize the fitness function; namely, it minimizes the errors between the calculated and experimental PEME performances.

3. Results and discussion

The results of the parameter estimation are presented first to illustrate the effectiveness of the proposed parameter estimation method. Subsequently, the effects of the ACL on PEME performance and its two-phase characteristics are discussed. Furthermore, the operation at a high cathode pressure is analyzed.

3.1 Parameter estimation

Parameter estimation was performed in our in-house experiments. Figure 2 shows a comparison of the polarization curves and ohmic impedances between the simulated and experimental results at three different temperatures. After the parameter estimation, the simulated results agreed well with the experimental data. The EIS results of the Nyquist plot at temperatures of 50℃, 65℃, and 80℃ for three current densities are shown in Figure 3. In the Nyquist plot, the ohmic impedance is caused by ion and electron transport, and it only presents

the resistance property without the capacitance property. Therefore, its imaginary part is zero, and the intersection point value of the real axis represents the ohmic impedance value. Because of the double-electrode layer effect, the activation impedance exhibited both resistance and capacitance properties. The first arc from the high-frequency section represents the activation impedance and its diameter reflects the value of the activation impedance. Mass transfer impedance is caused by inefficient mass transfer, such as liquid water supply and oxygen discharge in the anode, leading to a decrease in the liquid water content at the electrochemical reaction sites. The arc in the low-frequency section may appear under high-current-density conditions, representing mass transfer impedance. The EIS results have only one arc that represents the activation impedance in the low-current-density (0.2 A cm^{-2}) condition, and it shows the two arcs that represent the obvious activation and mass transfer impedance with increasing current density (from 0.6 and 1.0 A cm^{-2}). In our model, the mass transfer impedance is included in the activation impedance because the activation overpotential considers the effect of liquid water saturation, as shown in Eq. 16. As shown in Figure 2, the ohmic impedance decreased with increasing temperature owing to the increase in membrane conductivity. Increasing the temperature within a certain range also had a positive effect on reducing the activation impedance. The experimental results show that the activation impedance significantly decreases with increasing temperature from 50℃ to 65℃, while the decrease becomes less obvious with increasing temperature from 65℃ to 80℃. Moreover, we compared the EIS results at different current densities (see Supplementary Figure 3). The activation impedance decreased with increasing current density, which reflects the polarization

characteristics well, and the mass transfer impedance increased because of the greater liquid water consumption and higher oxygen production rates with increasing current density.

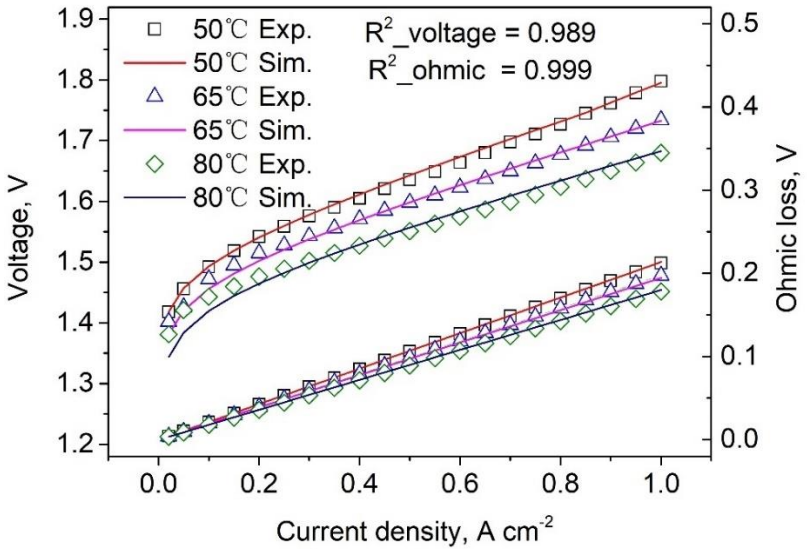

Figure 2. Results of parameter estimation validated with the in-house experiments: comparison of polarization curves and ohmic impedance between the simulation and experiment at temperatures of 50℃, 65℃, and 80℃.

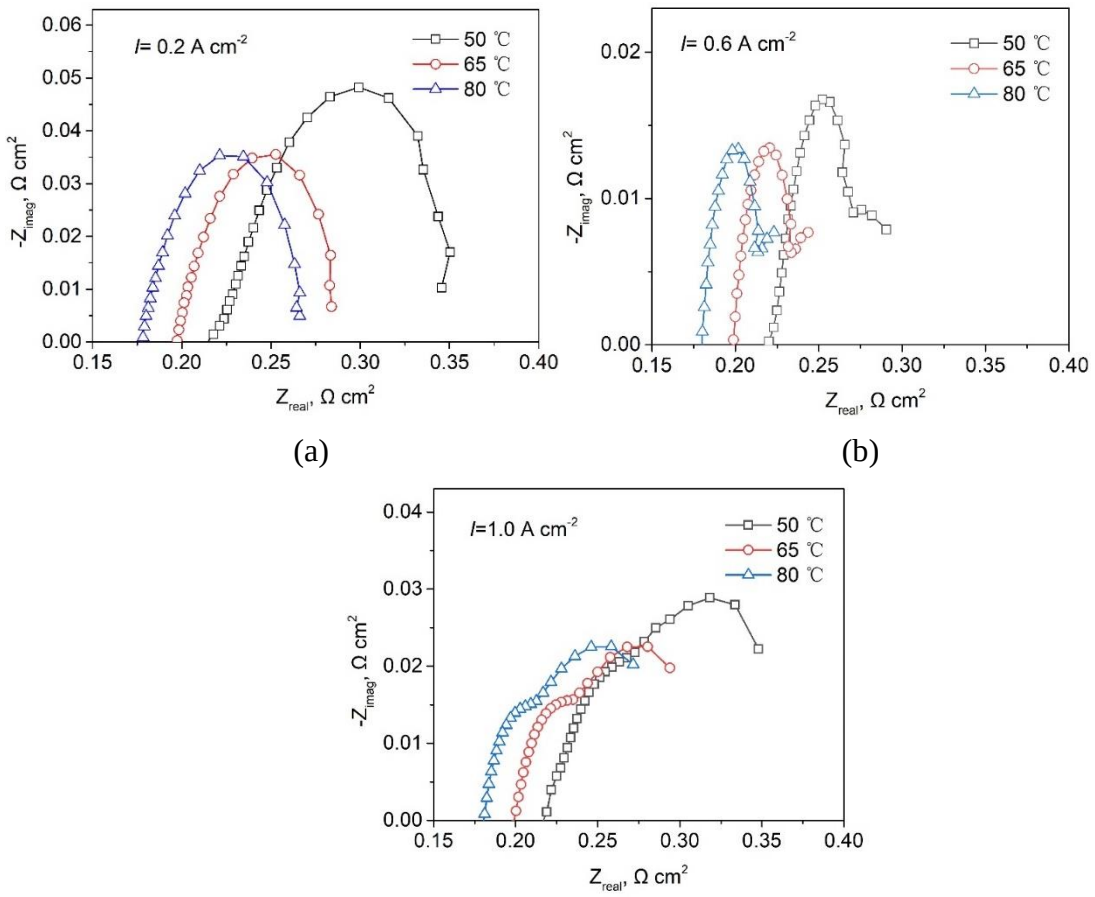

Figure 3. Comparison of EIS results at temperatures of 50℃, 65℃, and 80℃ and current densities of (a) 0.2 A cm^{-2}, (b) 0.6 A cm^{-2}, and (c) 0.8 A cm^{-2}.

In addition to our in-house experimental results, the proposed parameter estimation was further applied to the experimental results from six papers in the literature [26–31]. Marangio et al. [26] reported the experimental work on PEMEs under high-pressure cathode conditions. Figure 4 shows a comparison of the polarization curves between the simulation and the experiment from Ref. [26]; the validity of the results demonstrates the universal applicability of our developed PEME model and the parameter estimation method. The experimental details for modeling, including the membrane type, thickness, and porosity of the APTL, in the in-house experiments and Ref. [26] are listed in Table 1, and the corresponding values of the estimated parameters are listed in Table 2. Additional comparison results, including

polarization curves and/or ohmic impedance between the simulation and experiments, are shown in Supplementary Figures 4–8 [27–31], and good agreement is achieved. The experimental details and parameter estimation results in Refs. [27–31] are listed in Supplementary Tables 5 and 6, respectively.

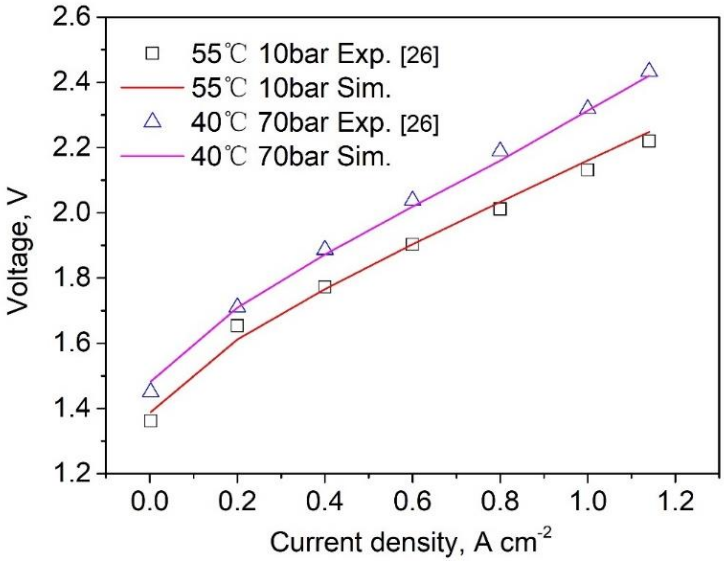

Figure 4. Results of parameter estimation validated with the experiments in Ref. [26]: comparison of polarization curves between the simulation and experiment at temperatures and cathode pressures of 55℃ and 10 bar and 40℃ and 70 bar.

Table 1. Experimental details for modeling [26].

Experimental source	Membrane	APTL thickness	APTL porosity
In-house (Figure 2)	Nafion 115	260 μm	0.5
Ref. [26] (Figure 4)	Nafion 117	/	/

Table 2. Parameter estimation results [26].

Experimental source	$i_{ref,a}$ (A m^{-2})	$i_{ref,a}$ (A m^{-2})	α_a	α_c	k_m	R_{con} (Ω m^2)
In-house (Figure 2)	9.163×10^{-3}	4.805×10^{3}	0.272	0.312	1.781	9.501×10^{-6}
Ref .[26] (Figure 4)	7.387×10^{-1}	5.865×10^{3}	0.1474	0.1477	1.169	3.109×10^{-5}

In summary, the effectiveness of the proposed parameter estimation method was demonstrated through in-house experiments and experiments reported in the literature.

3.2 ACL

The effects of the structural parameters of the APTL have been widely investigated [14,17], whereas the effects of the ACL have rarely been reported. In this section, the effects of ACL porosity, permeability, and thickness are investigated and discussed.

Figures 5(a), 5(b), and 5(c) show the polarization curves, efficiency, and liquid saturation at the interface of the ACL and membranes with different ACL porosities. The length of the through-plane direction in Figure 5(d) was rescaled for a better view because of the large differences in thickness between the different layers. As shown in Figure 5(a), the voltage of the PEME increases gradually with increasing current density under normal conditions; however, it may increase significantly when the current density reaches a certain value. From Figure 5(c), we can also see that the liquid saturation at the ACL–membrane interface decreases gradually with increasing current density and then drops to near zero. This current density is called the limiting current density of the PEME. The liquid water supply rate into the ACL and the oxygen discharge rate out of the ACL were insufficient, leading to severe reactant starvation at the limiting current density. Within the modeling range of the ACL porosities, increasing the ACL porosity increases the liquid saturation at the ACL–membrane interface and limit the current density. The limiting current densities are 0.5, 1.3, and 4.1 A cm^{-2} at ACL porosities of 0.2, 0.25, and 0.3. This would become >5.0 A cm^{-2} when further increasing the ACL

porosity, but note that this result is derived only from the view of mass transport and liquid saturation inside the ACL in our investigated range.

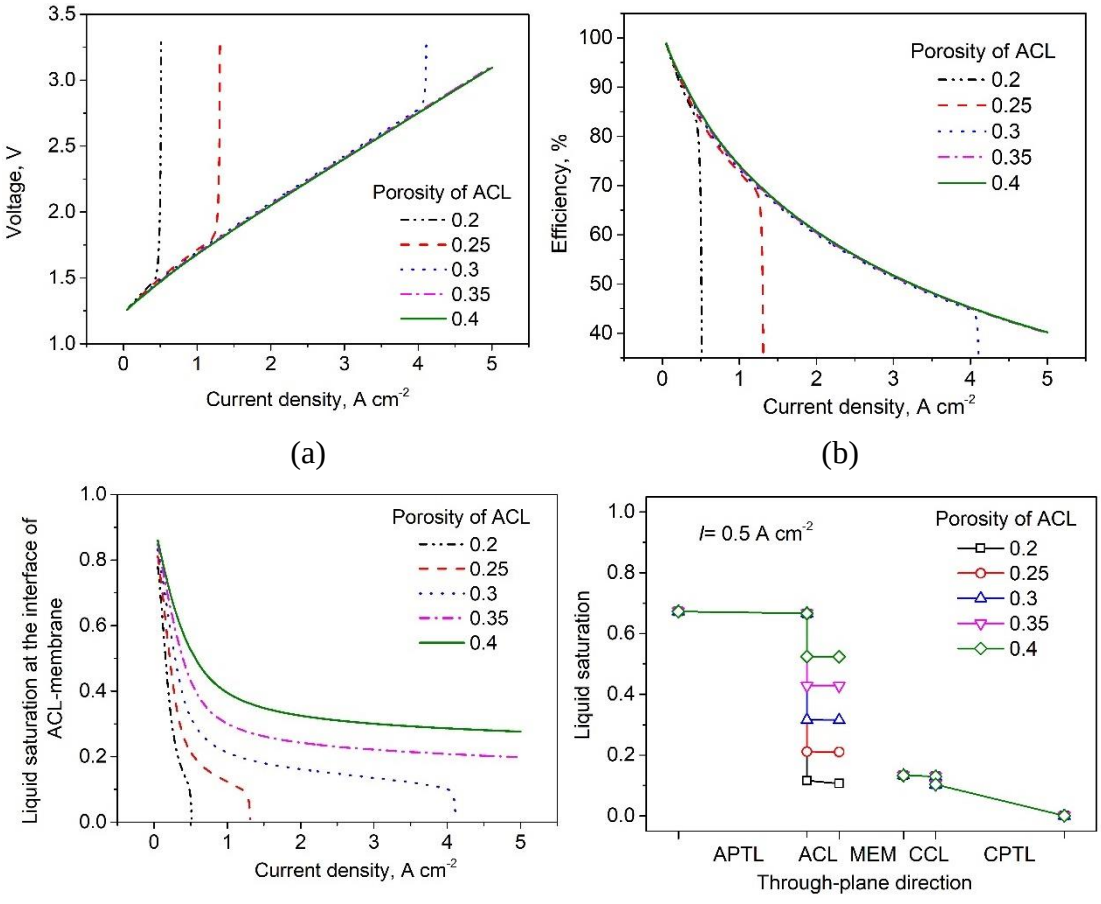

Figure 5. Effect of the ACL porosity: (a) polarization curves, (b) efficiency, (c) liquid saturation at the ACL–membrane interface, and (d) liquid saturation distribution at a current density of 0.5 A cm^{-2} with ACL porosities of 0.2, 0.25, 0.3, 0.35, and 0.4.

To better understand the porosity effect, observer the liquid saturation distribution at a current density of 0.5 A cm^{-2} with different ACL porosities, as shown in Figure 5(d). A liquid saturation jump at the interface between the APTL and ACL was clearly observed. The lower porosity of the ACL can lead to a sharp decrease in liquid saturation from the APTL side to the ACL side. According to the Leverett function of Eqs. 8 and 9, the capillary pressure is generally a decreasing function of the liquid saturation when the anode is hydrophilic. Consequently,

406 increasing ACL porosity can improve liquid saturation on the ACL side at the APTL–ACL
407 interface. Moreover, we can also find that the liquid saturation gradient inside the ACL is
408 insignificant. In other words, the liquid saturation jump effect was much more evident than the
409 effect of changing the liquid saturation gradient inside the ACL by changing the ACL porosity.
410 Figure 6 shows the effect of different ACL permeabilities on PEME performance.
411 Interestingly, both liquid saturation at the ACL–interface and the limiting current density
412 decreased with increasing ACL permeability. Figure 6(d) shows the liquid saturation
413 distribution at a current density of 0.5 A cm^{-2} with different ACL permeabilities. Decreasing
414 ACL permeability would increase the liquid transport resistance inside the ACL, while it would
415 increase the liquid saturation on the ACL side at the APTL–ACL interface caused by the liquid
416 saturation jump effect. Based on these results, the liquid saturation jump effect is more evident
417 than the effect of increasing the liquid transport resistance inside the ACL by decreasing the
418 ACL permeability. Meanwhile, although the liquid pressure decreased and the gas pressure
419 increased from the channel to the membrane along the through-plane direction in the anode
420 (see Supplementary Figure 10), the liquid saturation on the ACL side could still be higher than
421 that on the APTL side by properly adjusting the ACL permeability (to 1.0×10^{-12} m^2). It should
422 also be noted that permeability and porosity are two closely related parameters, and it is
423 difficult to alter one while keeping the other unchanged. Because of the complex internal
424 microstructure of CLs, the detailed numerical relationship between porosity and permeability
425 was not considered in this study. Therefore, Figures 5 and 6 only represent the effects of

porosity and permeability, which might lead to a much lower limiting current density in some cases.

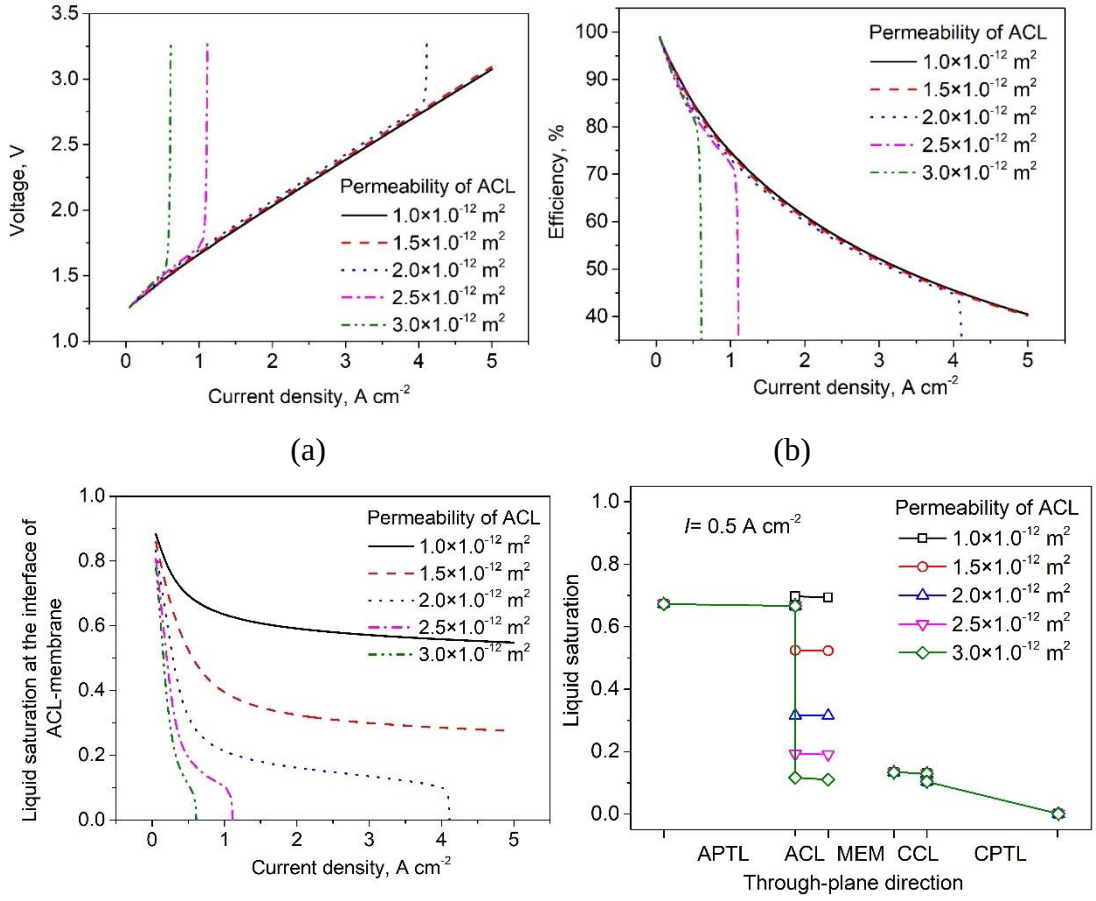

Figure 6. Effect of the ACL permeability: (a) polarization curves, (b) efficiency, (c) liquid saturation at the interface of the ACL and membrane, and (d) liquid saturation distribution at the current density of 0.5 A cm^{-2} with the ACL permeabilities of 1.0×10^{-12} m^2, 1.5×10^{-12} m^2, 2.0×10^{-12} m^2, 2.5×10^{-12} m^2, and 3.0×10^{-12} m^2.

Figure 7 shows the effect of different ACL thicknesses on PEME performance. The PEME voltage at a certain current density increased with increasing ACL thickness because the proton transport distance and ohmic impedance increased. Liquid saturation at the ACL–membrane interface and the limiting current density also decreased with increasing ACL thickness. Figure 7(d) shows the liquid saturation distribution at a current density of 2.0 A cm^{-2} with different ACL thicknesses. Note that the ACL thicknesses are different for the five cases, although the

points at the ACL–membrane interface have the same horizontal axis coordinates. The liquid saturation drop gradient inside the ACL increased with increasing ACL thickness owing to the greater transport distance. It should also be noted that the liquid saturation at the CCL–membrane interface is higher than that at the ACL–membrane interface because the water consumption rate in the anode and the crossover flux by EOD from the anode to the cathode are both high at a high current density.

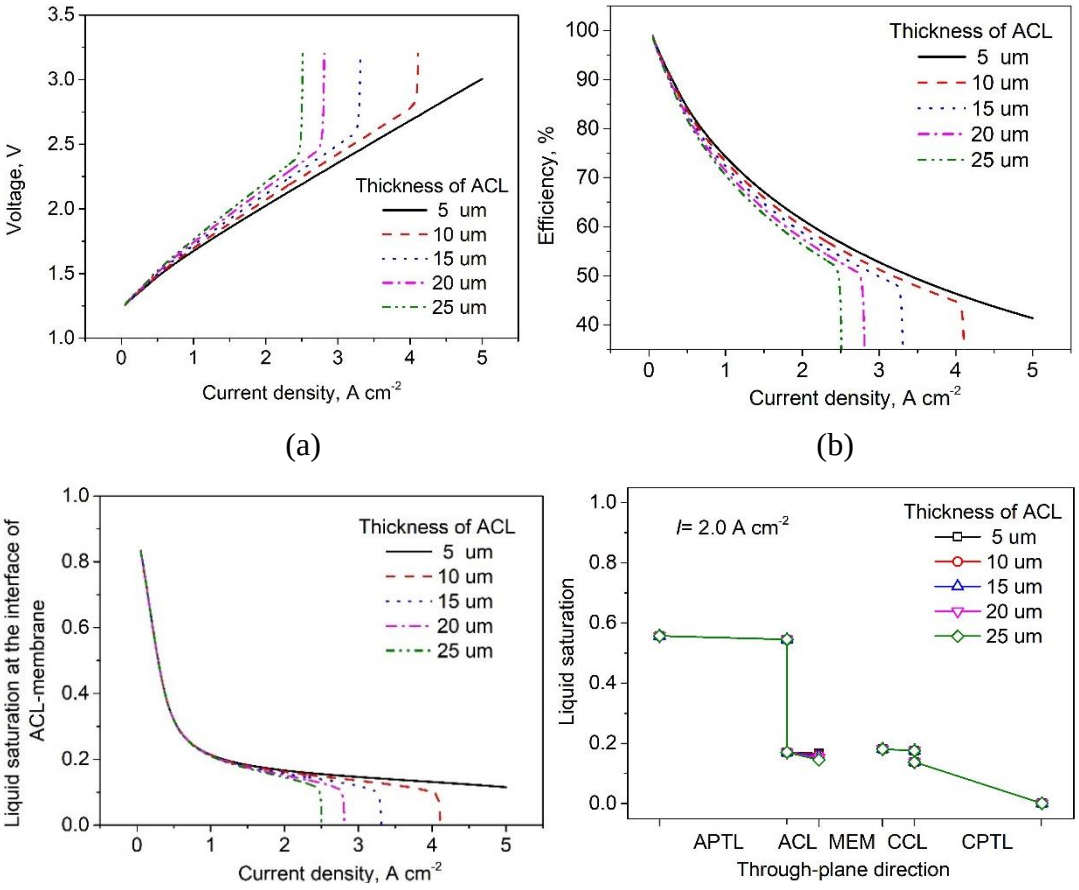

Figure 7. Effect of the ACL thickness: (a) polarization curves, (b) efficiency, (c) liquid saturation at the interface of the ACL and membrane, and (d) liquid saturation distribution at the current density of 2.0 A cm^{-2} with the ACL thicknesses of 5 μm, 10 μm, 15 μm, 20 μm, and 25 μm.

Overall, the results demonstrate that the effects of the ACL on the liquid saturation distribution and PEME performance, including the liquid saturation jump effect and mass and

proton transport inside the ACL, are critical and cannot be ignored, even though the thickness of the ACL is much less than that of the APTL.

3.3 Cathode high-pressure operation

The PEME cathode is usually under high pressure for the direct production of high-pressure hydrogen. This can save significant pump energy for hydrogen compression. In this section, the effects of cathode pressure and membrane permeability on PEME performance and its water transport characteristics during high-pressure cathode operation are discussed.

Figure 8(a)–8(d) show PEME performance and the liquid saturation distribution under cathode pressures of 1, 10, 30, and 50 bars, with the anode maintained at normal pressure (1 atm). First, the PEME voltage increased with increasing cathode pressure owing to the increased reversible voltage. More electrical energy is required to directly produce high-pressure hydrogen. Moreover, it should be noted that the limiting current density also increases with increasing cathode pressure. We found that liquid saturation at the ACL–membrane interface increased with increasing cathode pressure and decreased at the CL–membrane interface. Figures 8(e) and 8(f) show the water crossover flux from the anode to cathode at current densities of 2.0 and 4.0 A cm^{-2}. We found that the direction of total water crossover was from the anode to the cathode, and EOD was always dominant among the three mechanisms. The flux attributed to hydraulic permeation can be neglected even when the anode and cathode pressures are the same. This becomes obvious when the cathode pressure is increased to tens of bars and its direction is from the cathode to the anode. The EOD flux from the anode to the cathode increased almost linearly with the current density. The factor leading

to the limiting current density was a low or near-zero liquid saturation in the ACL with increasing current density. At a deeper level, the increasing water consumption rate from anode electrochemical reactions and the increasing water crossover flux from EOD with increasing current density simultaneously cause insufficient water in the ACL. Increasing the cathode pressure can promote water crossover from the cathode to the anode to improve the liquid saturation in the ACL. Diffusion flux is generally low because the ionomers in the anode and cathode are both in saturated vapor and the membrane water content difference is relatively small. In summary, increasing the cathode pressure can be viewed as an effective solution for water management inside a PEME, which can increase the limiting current density to a certain extent.

With the cathode high-pressure effect on PEME performance and water transport elucidated, the effect of membrane permeability can be easily explained. Figure 9 shows the results for different membrane permeabilities with the cathode pressure set to 10 bars. In cathode high-pressure operation, increasing the membrane permeability can improve water crossover by hydraulic permeation, which benefits water management inside the PEME and increases the limiting current density.

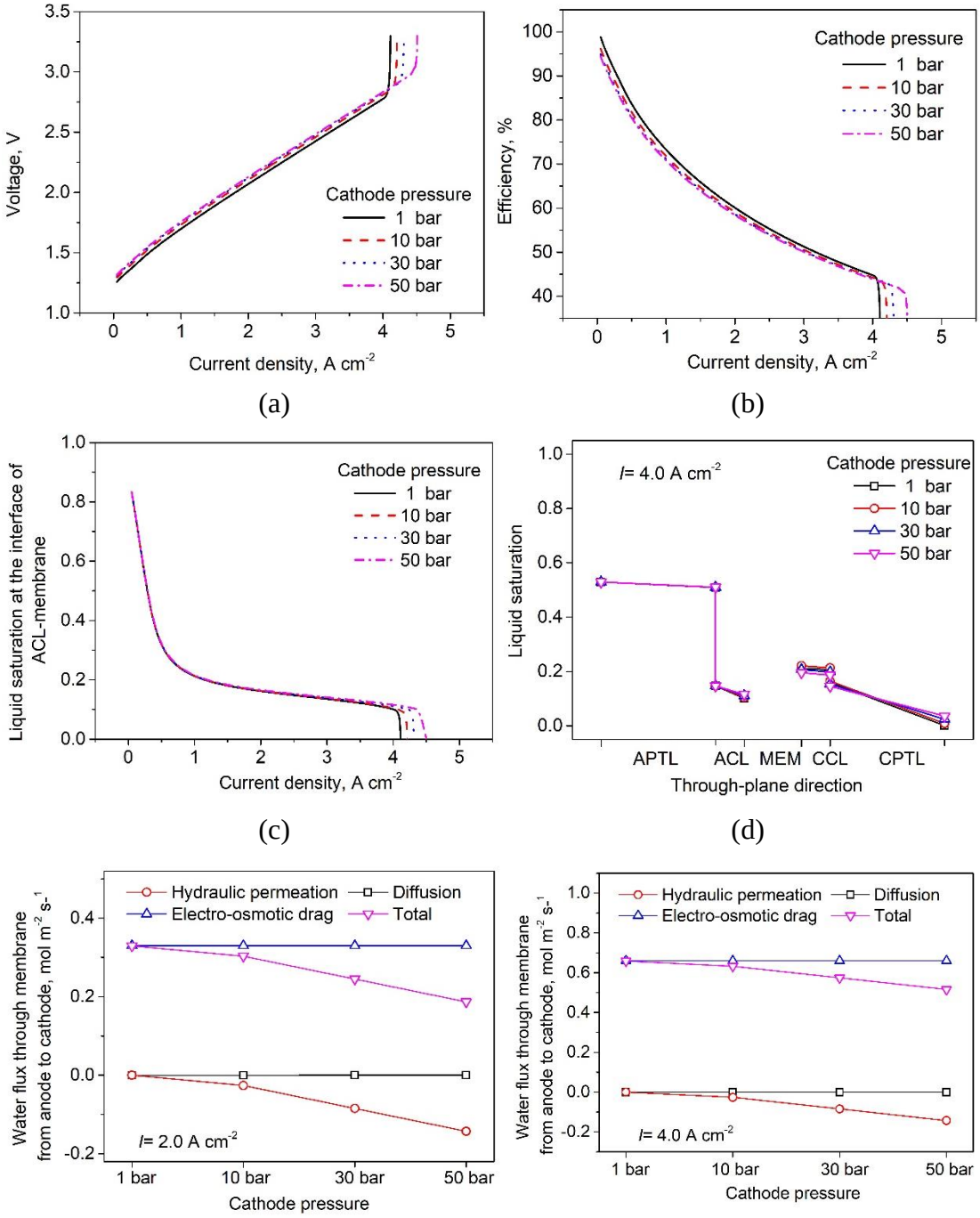

Figure 8. Effect of the cathode pressure in the high-pressure conditions: (a) polarization curves, (b) efficiency, (c) liquid saturation at the interface of the ACL and membrane, and (d) liquid saturation distribution at the current density of 4.0 A cm^{-2}; water crossover flux from the anode to cathode at the current densities of (e) 2.0 A cm^{-2}, and (f) 4.0 A cm^{-2} under the cathode pressure of 1 bar, 10 bar, 30 bar, and 50 bar.

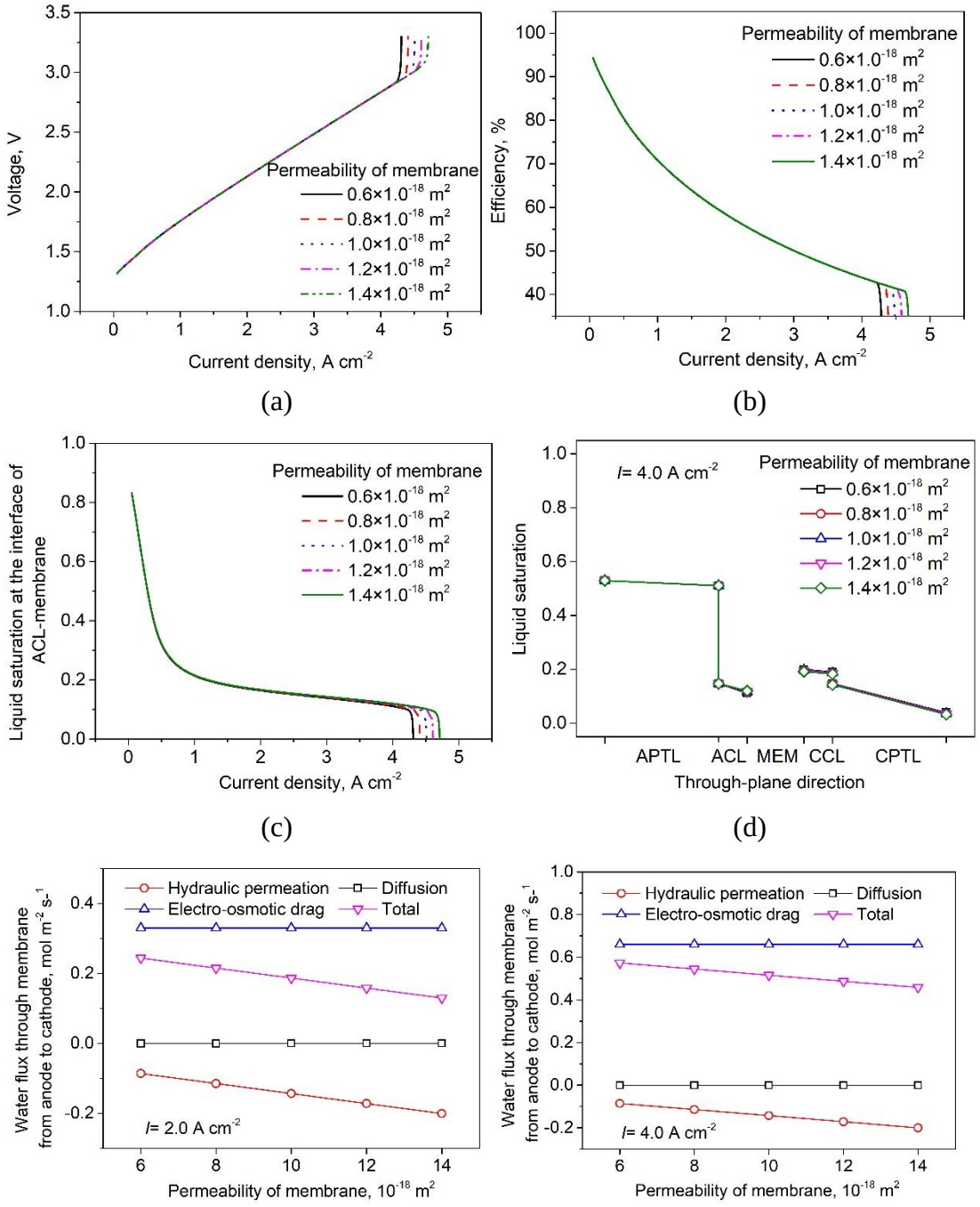

Figure 9. Effect of the membrane permeability in the high-pressure conditions: (a) polarization curves, (b) efficiency, (c) liquid saturation at the interface of the ACL and membrane, and (d) liquid saturation distribution at the current density of 4.0 A cm^{-2}; water crossover flux from the anode to cathode at the current densities of (e) 2.0 A cm^{-2}, and (f) 4.0 A cm^{-2} with the membrane permeabilities of 0.6×10^{-18} m^2, 0.8×10^{-18} m^2, 1.0×10^{-18} m^2, 1.2×10^{-12} m^2, and 1.4×10^{-18} m^2.

4. Conclusion

In this study, a two-phase analytical model of a PEME was developed that accounts for the liquid saturation jump effect. An intelligent method of parameter estimation using a GA was proposed to achieve high efficiency and automatic model validation. The effects of the ACL and high-pressure operation of the cathode on PEME performance and its two-phase characteristics were further investigated.

The EIS results from our in-house experiments showed that both ohmic and activation impedances decreased with increasing temperature and mass transfer impedance became obvious at a high current density. The proposed parameter estimation method was employed in in-house experiments and experiments from six papers in the literature, including polarization curves and ohmic impedances at different temperatures and under high-pressure operation. Very good agreement was achieved, and the effectiveness of the proposed parameter estimation method was demonstrated.

The PEME voltage might significantly increase when the current density reaches the limiting current density, and liquid saturation at the ACL–membrane interface would drop to nearly zero in this case. Increasing the ACL porosity increased the limiting current density within the investigated range through a mechanism in which the increasing ACL porosity improves liquid saturation on the ACL side at the APTL–ACL interface owing to the liquid saturation jump effect. Interestingly, the limiting current density increases with decreasing ACL permeability. This demonstrates that the liquid saturation jump effect on improving liquid saturation on the ACL side at the APTL–ACL interface is more obvious than the influence of

increasing the liquid transport resistance inside the ACL by decreasing ACL permeability. The limiting current density decreases with increasing ACL thickness. Therefore, the effects of the ACL on the liquid saturation distribution and PEME performance cannot be ignored, although the thickness of the ACL is much less than that of the APTL. The simulation results show that the limiting current density could reach >5 A cm^{-2} through proper design of the ACL parameters.

For high-pressure operation of the cathode, the limiting current density increased with increasing cathode pressure. EOD from the anode to the cathode is generally dominated by different water crossover mechanisms at normal pressure. At a high cathode pressure, the hydraulic permeation from the cathode to the anode was enhanced to improve liquid saturation in the ACL. The effects of membrane permeability on PEME performance were similar. Overall, increasing the cathode pressure and membrane permeability generally benefits water management inside the PEME and therefore increases the limit current density under cathode high-pressure operation. The methods proposed in this study and the detailed results can guide the design of cells and operating conditions for future PEME studies.

Acknowledgements

This research is funded by Hong Kong Scholars Program (No. XJ2021033), and China Postdoctoral Science Foundation (No. 2021TQ0235).

Declaration of Interests

The authors declare no competing interests.

Reference

[1] Dowell NM, Sunny N, Brandon N, Herzog H, et al. The hydrogen economy: A pragmatic path forward. Joule 2021; 5(10):2524-2529.

[2] Liu Z, Yi T, Huang C, Choy KL, Liu C. Thermodynamic and kinetics of hydrogen photoproduction enhancement by concentrated sunlight with CO2 photoreduction by heterojunction photocatalysts. Energy and AI 2021; 6:100102.

[3] Sun Y, Zheng W, Ji S, Sun A, et al. Dynamic behavior of high-temperature CO2/H2O co-electrolysis coupled with real fluctuating renewable power. Sustainable Energy Technol Assess, 2022; 52(D):102344.

[4] Ni M, Leung MKH, Leung DYC. Energy and exergy analysis of hydrogen production by a proton exchange membrane (PEM) electrolyzer plant. Energy Convers Manage 2008; 49(10):2748-2756.

[5] Yuan S, Zhao C, Cai X, An L, Shen S, et al. Bubble evolution and transport in PEM water electrolysis: Mechanism, impact, and management. Prog Energy Combust Sci 2023; 96:101075.

[6] Panchenko O, Borgardt E, Zwaygardt W, Hackemüller FJ, Bram M, et al. In-situ two-phase flow investigation of different porous transport layer for a polymer electrolyte membrane (PEM) electrolyzer with neutron spectroscopy. J Power Sources 2018; 390:108-115.

[7] Wang W, Yu S, Li K, Ding L, Xie Z, et al. Insights into the rapid two-phase transport dynamics in different structured porous transport layers of water electrolyzers through high-speed visualization. J Power Sources 2021; 516:230641.

585 [8] Majasan JO, Cho JIS, Dedigama I, Tsaoulidis D, Shearing P, et al. Two-phase flow
586 behaviour and performance of polymer electrolyte membrane electrolysers: Electrochemical
587 and optical characterization. Int J Hydrogen Energy 2018; 43:15659-15672.
588 [9] Kang Z, Mo J, Yang G, Retterer ST, Cullen DA, et al. Investigation of thin/well-tunable
589 liquid/gas diffusion layers exhibiting superior multifunctional performance in low-temperature
590 electrolytic water splitting. Energy Environ Sci 2017; 10, 166-175.
591 [10] Falcão D, Pinto A. A review on PEM electrolyzer modelling: Guidelines for beginners. J
592 Cleaner Prod 2020; 261:121184.
593 [11] Arbabi F, Montazeri H, Abouatallah R, Wang R, Bazylak A. Three-Dimensional
594 Computational Fluid Dynamics Modelling of Oxygen Bubble Transport in Polymer Electrolyte
595 Membrane Electrolyzer Porous Transport Layers. J Electrochem Soc 2016; 163 (11): F3062-
596 F3069.
597 [12] Wu L, Zhang G, Xie B, Tongsh C, Jiao K. Integration of the detailed channel two-phase
598 flow into three-dimensional multi-phase simulation of proton exchange membrane electrolyzer
599 cell. Int J Green Energy 2021; 18(6): 541-555.
600 [13] Xu Y, Zhang G, Wu L, Bao Z, Zu B, et al. A 3-D multiphase model of proton exchange
601 membrane electrolyzer based on open-source CFD. Digital Chem Eng 2021; 1:100004.
602 [14] Han B, Mo J, Kang Z, Yang G, Barnhill W, et al. Modeling of two-phase transport in
603 proton exchange membrane electrolyzer cells for hydrogen energy. Int J Hydrogen Energy
604 2017; 42: 4478-4489.

605 [15] Lee JK, Lee CH, Bazylak A. Pore network modelling to enhance liquid water transport
606 through porous transport layers for polymer electrolyte membrane electrolyzers. J Power
607 Sources 2019; 437: 226910.
608 [16] Sartory M, Wallnofer-Ogris E, Salman P, Fellinger T, Justl M, et al. Theoretical and
609 experimental analysis of an asymmetric high pressure PEM water electrolyser up to 155 bar.
610 Int J Hydrogen Energy 2017; 42: 30493-30508.
611 [17] García-Salaberri PA. 1D two-phase, non-isothermal modeling of a proton exchange
612 membrane water electrolyzer: An optimization perspective. J Power Sources 2020; 521:230915.
613 [18] Aouali FZ, Becherif M, Ramadan HS, Emziane M, Khellaf A, et al. Analytical modelling
614 and experimental validation of proton exchange membrane electrolyser for
615 hydrogen production. Int J Hydrogen Energy 2017; 42: 1366-1374.
616 [19] Hernández-Gómez Á, Ramirez V, Guilbert D, Saldivar B. Cell voltage static-dynamic
617 modeling of a PEM electrolyzer based on adaptive parameters: Development and experimental
618 validation. Renew Energy 2021; 163:1508-1522.
619 [20] Zhao D, He Q, Wu X, Xu Y, Jiang J, Li X, Ni M. Modeling and optimization of high
620 temperature proton exchange membrane electrolyzer cells. Int J Green Energy 2021;
621 DOI: 10.1080/15435075.2021.1974450.
622 [21] Wang Z, Wang X, Chen Z, Liao Z, et al. Energy and exergy analysis of a proton exchange
623 membrane water electrolysis system without additional internal cooling. Renew Energy 2021;
624 180:1333-1343.

[22] Abdin Z, Webb CJ, Gray EM. Modelling and simulation of a proton exchange membrane (PEM) electrolyser cell. Int J Hydrogen Energy 2015; 40:13243 -13257.

[23] Espinosa-Lopez M, Darras C, Poggi P, Glises R, Baucour P, et al. Modelling and experimental validation of a 46 kW PEM high pressure water electrolyzer. Renew Energy 2018; 119:160-173.

[24] Cheng C, Yang Z, Liu Z, Tongsh C, Zhang G, Xie B, He S, Jiao K. Numerical investigation on the feasibility of metal foam as flow field in alkaline anion exchange membrane fuel cell. Appl Energy 2021; 302:117555.

[25] Jiao K, Li X. Water transport in polymer electrolyte membrane fuel cells. Prog Energy Combust Sci, 2011; 37:221-291.

[26] Marangio F, Pagani M, Santarelli M, Cali M. Concept of a high pressure PEM electrolyser prototype. Int J Hydrogen Energy 2011; 36:7807-7815.

[27] K. Elsøe, Grahl-Madsen L, Scherer GG, Hjelm J, Mogensen MB. Electrochemical Characterization of a PEMEC Using Impedance Spectroscopy. J Electrochem Soc 2017;164 (13):F1419-F1426.

[28] Ito H, Maeda T, Nakano A, Hasegawa Y, Yokoi N, et al. Effect of flow regime of circulating water on a proton exchange membrane electrolyzer. Int J Hydrogen Energy 2010; 35:9550-9560.

[29] Lickert T, Kiermaier ML, Bromberger K, Ghinaiya J, Metz S, et al. On the influence of the anodic porous transport layer on PEM electrolysis performance at high current densities. Int J Hydrogen Energy 2020; 45:6047-6058.

[30] Ito H, Maeda T, Nakano A, Kato A, Yoshida T. Influence of pore structural properties of current collectors on the performance of proton exchange membrane electrolyzer. Electrochem Acta 2013; 100:242-248.

[31] Lee C, Lee JK, George MG, Fahy KF, LaManna JM, et al. Reconciling temperature-dependent factors affecting mass transport losses in polymer electrolyte membrane electrolyzers. Energy Convers Manage 2020; 213:112797.

Figure and table captions

Figure 1. Schematic of the PEME model and basic materials.

Figure 2. Results of parameter estimation validated with the in-house experiments: comparison of polarization curves and ohmic impedance between the simulation and experiment at temperatures of 50℃, 65℃, and 80℃.

Figure 3. Comparison of EIS results at temperatures of 50℃, 65℃, and 80℃ and current densities of (a) 0.2 A cm^{-2}, (b) 0.6 A cm^{-2}, and (c) 0.8 A cm^{-2}.

Figure 4. Results of parameter estimation validated with the experiments in Ref. [26]: comparison of polarization curves between the simulation and experiment at temperatures and cathode pressures of 55℃ and 10 bar and 40℃ and 70 bar.

Figure 5. Effect of the ACL porosity: (a) polarization curves, (b) efficiency, (c) liquid saturation at the ACL–membrane interface, and (d) liquid saturation distribution at a current density of 0.5 A cm^{-2} with ACL porosities of 0.2, 0.25, 0.3, 0.35, and 0.4.

Figure 6. Effect of the ACL permeability: (a) polarization curves, (b) efficiency, (c) liquid saturation at the interface of the ACL and membrane, and (d) liquid saturation distribution at

667 the current density of 0.5 A cm^{-2} with the ACL permeabilities of 1.0×10^{-12} m^2, 1.5×10^{-12} m^2,
668 2.0×10^{-12} m^2, 2.5×10^{-12} m^2, and 3.0×10^{-12} m^2.

669 Figure 7. Effect of the ACL thickness: (a) polarization curves, (b) efficiency, (c) liquid
670 saturation at the interface of the ACL and membrane, and (d) liquid saturation distribution at
671 the current density of 2.0 A cm^{-2} with the ACL thicknesses of 5 μm, 10 μm, 15 μm, 20 μm,
672 and 25 μm.

673 Figure 8. Effect of the cathode pressure in the high-pressure conditions: (a) polarization curves,
674 (b) efficiency, (c) liquid saturation at the interface of the ACL and membrane, and (d) liquid
675 saturation distribution at the current density of 4.0 A cm^{-2}; water crossover flux from the anode
676 to cathode at the current densities of (e) 2.0 A cm^{-2}, and (f) 4.0 A cm^{-2} under the cathode
677 pressure of 1 bar, 10 bar, 30 bar, and 50 bar.

678 Figure 9. Effect of the membrane permeability in the high-pressure conditions: (a) polarization
679 curves, (b) efficiency, (c) liquid saturation at the interface of the ACL and membrane, and (d)
680 liquid saturation distribution at the current density of 4.0 A cm^{-2}; water crossover flux from the
681 anode to cathode at the current densities of (e) 2.0 A cm^{-2}, and (f) 4.0 A cm^{-2} with the membrane
682 permeabilities of 0.6×10^{-18} m^2, 0.8×10^{-18} m^2, 1.0×10^{-18} m^2, 1.2×10^{-12} m^2, and 1.4×10^{-18}
683 m^2.

684 Table 1. Experimental details for modeling [26].

685 Table 2. Parameter estimation results [26].